Gas absorption into a spherical liquid droplet: numerical and theoretical study

C. Wylock, P. Colinet, B. Haut

PII: S1385-8947(12)00987-4
DOI: http://dx.doi.org/10.1016/j.cej.2012.07.085
Reference: CEJ 9600

To appear in: *Chemical Engineering Journal*

Please cite this article as: C. Wylock, P. Colinet, B. Haut, Gas absorption into a spherical liquid droplet: numerical and theoretical study, *Chemical Engineering Journal* (2012), doi: http://dx.doi.org/10.1016/j.cej.2012.07.085

Gas absorption into a spherical liquid droplet: numerical and theoretical study

C. Wylock[*,a], P. Colinet[a], B. Haut[a]

[a]Transfers, Interfaces and Processes (TIPs),Université Libre de Bruxelles, 50 av. F.D. Roosevelt CP 165/67, 1050 Brussels, Belgium

Abstract

This work deals with the modeling and the direct numerical simulation of the absorption of a gas component into a spherical liquid droplet in free fall, where the absorbed component takes part to a chemical reaction. This study is realized by computing the flow fields and the concentration fields simultaneously in the gas and liquid phases. The time evolution of the droplet global mass absorption rate is studied for various regimes characterized by the Reynolds and the Hatta numbers. The monitoring of the time evolution of the concentration fields in the droplet enables the understanding of the interactions between the diffusive and convective mass transports and the chemical reaction. The phenomena controlling the mass transfer rate and how they evolve during the mass absorption process can then be identified. In a first stage, the case of the physical absorption is studied. Moreover, analytical expressions are developed to correlate the time evolution of the Sherwood number with the Reynolds number and the absorption time. In a second stage, the influence of the coupling with a chemical reaction is studied. It is observed that several rate-limiting mechanisms successively control the global absorption rate, enlightening the complex interactions between convective and diffusive mass transport and the chemical reaction.

Key words: droplet, mass transfer, chemical reaction, computational fluid dynamics

*Corresponding author

Email address: cwylock@ulb.ac.be (C. Wylock)

Preprint submitted to Chemical Engineering Journal *July 10, 2012*

1. Introduction

The absorption of gas materials from flue gas by reactive liquid droplets is an important mass transfer process for several industrial applications, such as air pollution control. The presence of a chemical component in the liquid phase which reacts with the absorbed component enables a considerable enhancement of the mass transfer rate. One of the most studied case is the scrubbing of sulfur dioxide (SO_2) by a limestone slurry in a counter current spray scrubber, used in order to reduce the emissions [1, 2, 3, 4]. A deep understanding of the phenomena taking place during the gas-droplet mass transfer coupled with chemical reaction is of fundamental interest for the design and the optimization of such industrial applications.

A detailed modeling, based on a sound mathematical statement, is required to predict correctly the gas-droplet mass transfer rate and its evolution over time. This is a complex problem, as shown by the large number of mathematical models and experimental investigations that have been devoted to it. Indeed, the mass transfer rate is influenced by several phenomena and by their intricate couplings: the diffusive transport, the convective transport imposed by the flow fields in both phases, and the chemical reaction in the liquid phase.

This complexity is probably one of the main reason explaining why many empirical and idealized models can be found in the literature. For instance, the expression for the Sherwood number derived by Frössling from a study of the evaporation of small water droplet (see [5]) was often used for gas absorption into a droplet. More recently, Brogren and Karlsson [1] have proposed a model for the flue gas desulfurization taking into account all the chemical reactions taking place in the liquid but using the Higbie penetration theory [6] for the mass transport.

Nowadays, it is well known that for falling droplets having a Reynolds number (defined in section 2.2) higher than 10, the shear stress exerted by the gas phase induces a vortex in the droplet [7], which can have a significant influence on the mass transfer rate [8, 9, 10]. To compute the flow field in both phases and their influence on the mass transfer is one of the main modeling difficulty, which has been studied for decades.

It is now commonly admitted that, for Reynolds numbers smaller than 1, the gas flow is creeping and the flow field in the droplet can be described by the analytical stream function of Hadamard and Rybczinski [7, 11]. For higher Reynolds numbers, between 1 and 80, the stream function determined by the approximate expressions of Hameliec and Johnson [12] can be used instead. Leclair et al. [7] presented a general theoretical framework to compute the flow fields inside and outside water droplets. One of the first works to compute the mass mass transfer rate with internal circulation was realized by Kronig and Brink [13] in the framework of extraction. The first incorporation of the flow fields computed using the model of Leclair et al. [7] into a model of gas absorption was realized by Baboolal et al. [14], as mentioned by Elperin and Fominykh [15]. The work of Uribe-Ramírez and Korchinsky [16] presented a theory yielding an analytical solution for the mass transfer rate at intermediate Reynolds number. In the most recent works, an increasing numbers of authors used Computational Fluid Dynamics to compute the flow fields in both phases, such as in works of Waheed et al. [17], or Paschedag et al. [18].

This work proceeds along these lines, dealing with the modeling and the direct numerical simulation of the absorption of a component A from a gas phase into a spherical liquid droplet in free fall in this gas phase. A component B is dissolved in the liquid droplet and reacts with A following this irreversible reaction:

$$A + B \rightarrow C \qquad (1)$$

where C is the product of the reaction.

This study is realized by computing the flow fields and the concentration fields simultaneously in both the gas and liquid phases. This enables to rigorously account for the coupling between convection, diffusion and reaction. This work is focused on water droplet falling in air but the model equations are presented in a general dimensionless form, making the model suitable for studying mass transfer in other systems.

This work has two main goals. The first one is the detailed study of the time evolution of the droplet global mass absorption rate for various flow regimes and chemical regimes, which are characterized by the Reynolds number (defined in section 2.2) and the Hatta number (defined in section 2.3), respectively. The monitoring of the time evolution of the concentration fields in the droplet yields a better understanding of the influence of the interactions between the diffusive/convective mass transport and chemical reaction on the time evolution of the mass transfer rate. This procedure enables the identification, for each regime, of the phenomena controlling the mass transfer rate and how they possibly evolve during the mass absorption. The second goal is to propose analytical expressions to estimate the time evolution of the droplet mass transfer rate in the case of

physical absorption (no chemical reaction). This is realized by comparing the simulation results with simplified modelling approaches based on the analysis of the mass transfer rate-limiting phenomena.

2. Mathematical statement

2.1. Assumptions

This work is focused on the case of a spherical water droplet of constant volume in free fall in air. It is considered that the droplet falls at its terminal velocity and that its motion is rectilinear with a non-deformable interface. The two phases are considered incompressible and the flows in both phases are assumed to be stationary, laminar and axisymmetric. It is considered that the interface is completely free from surface-active contaminants and the continuity of the velocity and of the tangential shear stress is considered at the interface (in particular, possible Marangoni effects due to surface tension variations are neglected). In addition, it is considered that the mass absorption and the resulting chemical reactions in the liquid phase do not significantly affect the density and the viscosity of the two phases. With these assumptions, the continuity and momentum transport equations can be solved separately from the mass transport equations.

The assumption of stationary flow is justified by the fact that the characteristic time of the transient droplet motion is much smaller than the characteristic time of diffusive mass transport, since the Schmidt number (defined in section 2.3) is much larger than one.

According to Elperin and Fominykh [15], a spherical shape of a droplet falling in a gas phase is observed until a Reynolds number of 300, which corresponds approximately to a droplet diameter of 1.1 mm for a water droplet falling in air. This limit is also mentioned for limestone droplets by Akbar et al. [19]: the droplets remain spherical until 1 mm and their interface is non-oscillating until a Reynolds number between 300 and 400. Beyond this value, the droplet starts to be deformed and their interface oscillates. This value is also presented as an upper limit for the spherical shape in the numerical study performed by Amokrane and Caussade [20]. Clift et al. [21] reported that water droplets smaller than 1 mm falling in air can be considered as rigid spheres. Other authors, such as

Bandyopadhyay and Biswas [2], claim that water droplets falling in gas are spherical and their interface is non-oscillating until a diameter of 0.5 mm but that this has no significant influence on the mass transfer rate at this stage since the effects of the oscillation of the interface and its deformation on the mass transfer mutually compensate each other. Therefore, it appears that the assumptions of a spherical shape and a non-deformable interface are valid, for water droplets in air, until a diameter of 1 mm, corresponding to a Reynolds number of 250.

Concerning the laminar flow assumption, Amokrane and Caussade [20] evaluated that for droplets of water falling in air, the flow becomes turbulent in both gas and liquid phases for a diameter close to 1.6 mm. It corresponds to a Reynolds number close to 690 in the assumption of a rigid sphere. Moreover, according to Paschedag et al. [18], the flow of the gas phase around a droplet is a creeping flow until a Reynolds number of 0.1. For higher values, wakes are formed behind the droplet but the flow remains laminar until a Reynolds number of 500.

The validity limit for the axisymmetric assumption appears to be a diameter of 1 mm for water droplets falling in air at their terminal velocity, according to Walcek et al. [22] (and cited by Altwicker and Lindhjem [23]), which claim that the internal circulation pattern is steady and that the absorption characteristics follow the model of Kroning and Brink [13].

Therefore, taking into account this literature review, the assumptions of the developed model are valid for $Re \leq 250$. In addition, in order to prevent too large numerical errors of the simulation, the minimum considered Reynolds number is 0.01. It corresponds, for water droplet falling in air, to a droplet diameter of 17 µm.

The model is based on the balance equations written in dimensionless form in an inertial reference frame attached to the center of mass of the droplet. A two-dimensional axisymmetric computational domain is used. It is presented schematically in Fig. 1. This computational domain is divided in two distinct subdomains: one for the gas phase and one for the liquid phase. The droplet diameter d_d is used as the reference length. Therefore, the dimensionless radius of the droplet is 0.5. A domain diameter 10 times larger than the droplet is used in this work. In the reference frame, the gas is flowing upward. r and z are the dimensionless radial and axial component of the cylindrical coordinate system, respectively.

Fig. 1

2.2. Flow fields

The flow fields are computed by solving the stationary incompressible Navier-Stokes and continuity equations in both gas and liquid phases.

The droplet diameter d_d is used as the reference length and the terminal falling velocity U is used as the reference velocity. The reference pressure is

defined as $\rho_g U^2$, where ρ_g is the gas density. The Reynolds number is defined as $\mathrm{Re} = \rho_g d_d U/\eta_g$, where η_g is the gas dynamic viscosity.

In both phases, let $\mathbf{u} = (u, v)$ be the dimensionless velocity and p the dimensionless pressure. The subscript l and g are used to refer to the liquid and the gas phases, respectively.

The Navier-Stokes and continuity equations in the gas phase read:

$$u_g \frac{\partial u_g}{\partial r} + v_g \frac{\partial u_g}{\partial z} = -\frac{\partial p_g}{\partial r} + \frac{1}{\mathrm{Re}}\left(\frac{\partial^2 u_g}{\partial r^2} + \frac{1}{r}\frac{\partial u_g}{\partial r} - \frac{u_g}{r^2} + \frac{\partial^2 u_g}{\partial z^2}\right) \quad (2)$$

$$u_g \frac{\partial v_g}{\partial r} + v_g \frac{\partial v_g}{\partial z} = -\frac{\partial p_g}{\partial z} + \frac{1}{\mathrm{Re}}\left(\frac{\partial^2 v_g}{\partial r^2} + \frac{1}{r}\frac{\partial v_g}{\partial r} + \frac{\partial^2 v_g}{\partial z^2}\right) \quad (3)$$

$$\frac{\partial u_g}{\partial r} + \frac{u_g}{r} + \frac{\partial v_g}{\partial z} = 0 \quad (4)$$

while the Navier-Stokes and continuity equations in the liquid phase are:

$$\rho^*\left(u_l \frac{\partial u_l}{\partial r} + v_l \frac{\partial u_l}{\partial z}\right) = -\frac{\partial p_l}{\partial r} + \frac{\eta^*}{\mathrm{Re}}\left(\frac{\partial^2 u_l}{\partial r^2} + \frac{1}{r}\frac{\partial u_l}{\partial r} - \frac{u_l}{r^2} + \frac{\partial^2 u_l}{\partial z^2}\right) \quad (5)$$

$$\rho^*\left(u_l \frac{\partial v_l}{\partial r} + v_l \frac{\partial v_l}{\partial z}\right) = -\frac{\partial p_l}{\partial z} + \frac{\eta^*}{\mathrm{Re}}\left(\frac{\partial^2 v_l}{\partial r^2} + \frac{1}{r}\frac{\partial v_l}{\partial r} + \frac{\partial^2 v_l}{\partial z^2}\right) \quad (6)$$

$$\frac{\partial u_l}{\partial r} + \frac{u_l}{r} + \frac{\partial v_l}{\partial z} = 0 \quad (7)$$

where $\rho^* = \rho_l/\rho_g$ and $\eta^* = \eta_l/\eta_g$ are the density and the dynamic viscosity ratios, respectively.

At the droplet interface, which is considered completely free from surface-active contaminants, it is assumed, on the one hand, that the component of the shear stress tangent to the interface is continuous across the interface. On the other hand, the balance of the component of the shear stress normal to the interface is unnecessary since the interface is considered as non-deformable. Therefore, the following equation is written:

$$\left(2\frac{\partial u_g}{\partial r} n_r t_r + \left(\frac{\partial u_g}{\partial z} + \frac{\partial v_g}{\partial r}\right)(n_r t_z + n_z t_r) + 2\frac{\partial v_g}{\partial z} n_z t_z\right) = \eta^*\left(2\frac{\partial u_l}{\partial r} n_r t_r + \left(\frac{\partial u_l}{\partial z} + \frac{\partial v_l}{\partial r}\right)(n_r t_z + n_z t_r) + 2\frac{\partial v_l}{\partial z} n_z t_z\right) \quad (8)$$

where $\mathbf{n} = (n_r, n_z)$ and $\mathbf{t} = (t_r, t_z)$ are unit vectors, normal and tangent to the interface, respectively.

In addition, it is assumed, at the droplet interface, that the component of the velocity tangent to the interface is continuous across the interface and that the component of the velocity normal to the interface equals zero in both phases:

$$u_g n_r + v_g n_z = u_l n_r + v_l n_z = 0 \quad (9)$$

$$u_g t_r + v_g t_z = u_l t_r + v_l t_z \quad (10)$$

At the top boundary of the domain, corresponding to the gas flow outlet, a free flow outlet boundary condition is imposed. The resulting equations write:

$$p_g = 0 \quad (11)$$

$$\frac{1}{\mathrm{Re}}\left(2\frac{\partial u_g}{\partial r} n_r + \left(\frac{\partial u_g}{\partial z} + \frac{\partial v_g}{\partial r}\right) n_z\right) = 0 \quad (12)$$

$$\frac{1}{\mathrm{Re}}\left(\left(\frac{\partial u_g}{\partial z} + \frac{\partial v_g}{\partial r}\right) n_r + 2\frac{\partial v_g}{\partial z} n_z\right) = 0 \quad (12)$$

At the bottom boundary of the domain, corresponding to the gas flow inlet, a uniform upward velocity is imposed:

$$u_g = 0 \quad (14)$$

$$v_g = 1 \quad (15)$$

2.3. Concentration fields

Since the mass transfer resistance can evolve with time due to the competition between convection, diffusion and reaction phenomena, the concentration fields are computed by solving the transient mass transport equations in both phases, imposing the gas-liquid equilibrium and the continuity of the mass transfer rate of the component A at the interface.

The reference time τ is defined as $\tau = d_d/U$. Let $[A]_{eq}$ be the concentration of A in the droplet when the equilibrium with the gas phase is reached. Considering dilute liquid solution and perfect gas, $[A]_{eq}$ is defined as $[A]_{eq} = h[A_g]_\infty$. $[A_g]_\infty$ is the concentration of A in the gas phase far from the droplet and $h = HRT$, where H is the Henry, R is the perfect gas constant and T is the absolute temperature. Let $[B]_0$ be the initial concentration of B in the droplet.

$[A]_{eq}$ is used as the reference concentration of A, in both the gas and liquid phases, while $[B]_0$ is used as the reference concentration for B.

Let t be the dimensionless time. Let C_{A_g} be the dimensionless concentration of A in the gas phase. C_A and C_B are the dimensionless concentrations of A and B in the liquid phase, respectively.

As there is no chemical reaction in the gas phase, the following mass transport equation, involving only diffusive and convective transports, is considered for A in the gas phase:

$$\frac{\partial C_{A_g}}{\partial t} + u_g\frac{\partial C_{A_g}}{\partial r} + v_g\frac{\partial C_{A_g}}{\partial z} = \frac{\beta_g}{\mathrm{Pe}}\left(\frac{\partial^2 C_{A_g}}{\partial r^2} + \frac{1}{r}\frac{\partial C_{A_g}}{\partial r} + \frac{\partial^2 C_{A_g}}{\partial z^2}\right) \quad (16)$$

where $\beta_g = \mathbb{D}_{A_g}/\mathbb{D}_{A_l}$ and $\mathrm{Pe} = U d_d/\mathbb{D}_{A_l}$. Pe is the Peclet number for the mass transport of A in the liquid phase. Note that this Peclet number can be calculated from the Reynolds number and the Schmidt number $\mathrm{Sc} = \eta_l/\rho_l\mathbb{D}_{A_l}$ of A in the liquid by $\mathrm{Pe} = \mathrm{Re}\,\mathrm{Sc}\,\rho^*/\eta^*$.

Two mass transport equations, involving diffusion, convection and chemical reaction, are considered for A and B in the liquid phase. They write:

$$\frac{\partial C_A}{\partial t} + u_l\frac{\partial C_A}{\partial r} + v_l\frac{\partial C_A}{\partial z} = \frac{1}{\mathrm{Pe}}\left(\frac{\partial^2 C_A}{\partial r^2} + \frac{1}{r}\frac{\partial C_A}{\partial r} + \frac{\partial^2 C_A}{\partial z^2}\right) - \psi \quad (17)$$

$$\frac{\partial C_B}{\partial t} + u_l\frac{\partial C_B}{\partial r} + v_l\frac{\partial C_B}{\partial z} = \frac{\beta_b}{\mathrm{Pe}}\left(\frac{\partial^2 C_B}{\partial r^2} + \frac{1}{r}\frac{\partial C_B}{\partial r} + \frac{\partial^2 C_B}{\partial z^2}\right) - \chi\psi \quad (18)$$

where $\chi = h[A_g]_\infty/[B]_0$ is the concentration ratio between the maximum concentration of A that can be reached in the droplet and the initial concentration of the B in the droplet and $\beta_b = \mathbb{D}_B/\mathbb{D}_{A_l}$. ψ is the dimensionless chemical reaction rate.

It is assumed that the reaction (see Eq. (1)) is of the first order with respect to the concentrations of A and B, and that its kinetic constant is k. Therefore, ψ is calculated by:

$$\psi = \mathrm{Ha}^2 C_A C_B \quad (19)$$

where $\mathrm{Ha} = \sqrt{k[B]_0 \tau}$ is the Hatta number.

The Hatta number compares the reference time τ to the characteristic time of the reaction [24, 25]. A Hatta number lower than unity means that the reaction is slow compared to the convective time scale τ. When the Hatta number is of order one, the chemical reaction rate and τ have the same order of magnitude. Finally, when the Hatta number is larger than one, the reaction occurs much faster than the time it takes for the droplet to travel a distance equal to its diameter.

At the droplet interface, the gas-liquid equilibrium for A and the continuity across the interface of the flux of A normal to the interface are assumed. Therefore, the following boundary conditions can be written:

$$C_A = hC_{A_g} \quad (20)$$

$$\frac{\partial C_A}{\partial r} n_r + \frac{\partial C_A}{\partial z} n_z = \beta_g \left(\frac{\partial C_{A_g}}{\partial r} n_r + \frac{\partial C_{A_g}}{\partial z} n_z \right) \quad (21)$$

It is assumed that B does not cross the droplet interface. Therefore, the following no flux boundary condition can be written:

$$\frac{\partial C_B}{\partial r} n_r + \frac{\partial C_B}{\partial z} n_z = 0 \quad (22)$$

At the top boundary, it is assumed that the transport of A is only convective. Therefore, the top boundary condition reads:

$$\frac{\partial C_{A_g}}{\partial r} n_r + \frac{\partial C_{A_g}}{\partial z} n_z = 0 \quad (23)$$

At the bottom boundary, a uniform concentration of A entering the gas subdomain is assumed:

$$C_{A_g} = h^{-1} \quad (24)$$

At the initial time $t = 0$, it is supposed that the concentrations in both phases are homogeneous and at equilibrium in the liquid phase. The initial conditions for the concentrations write therefore:

$$C_{A_g}(t = 0) = h^{-1} \quad (25)$$

$$C_A(t = 0) = \alpha \quad (26)$$

$$C_B(t = 0) = 1 \quad (27)$$

$\alpha = [A]_0 / h[A_g]_\infty$ is the ratio between the initial concentration of A in the droplet, denoted $[A]_0$, and the maximum concentration of A that can be reached in the droplet.

3. Simulations

The equations of the model are solved numerically using the COMSOL Multiphysics 3.4 software. This commercial code uses the finite element method to solve the boundary-value problem. The “Incompressible Navier-Stokes mode”

coupled with the “Convection and Diffusion mode”, of the “Chemical Engineering Module”, are used in a 2D axisymmetric geometry.

Since finite elements are used, a meshing of the computational domain has to be defined. The equations are discretized using quadratic Lagrangian elements.

3.1. Meshing

The two subdomains are meshed independently and so-called boundary-layer meshes are used in both gas and liquid phases near the interface. This mesh type is characterized by the coexistence of two mesh shapes in the domain. On the domain zones which are characterized by the presence of very important gradients, such as in boundary layers, rectangular shape meshes are used. Triangular shape meshes are used outside these zones, in the bulk of the phases.

In the liquid subdomain (on the left in Fig. 2), a boundary-layer mesh is defined near the interface boundary and near the symmetry axis. This boundary-layer zone contains 1080 meshes. It is made of a layer of 15 rectangles with a stretching factor equal to 1.15 in the direction normal to the interface and the symmetry axis, towards the droplet interior. The first layer is made of 44 rectangles, regularly spaced along the interface and 28 rectangles regularly spaced along the symmetry axis. The thickness of the first layer equals $7.5\ 10^{-4}$. The remaining subdomain is meshed with 880 triangular meshes.

Fig. 2

In the gas subdomain (on the right in Fig. 2), a boundary-layer mesh is defined near the gas-liquid interface. This boundary-layer zone contains 280 meshes. It is made of a layer of 20 rectangles with a stretching factor equal to 1.2 in the direction normal to the interface, towards the bulk of the gas phase. The first layer is made of 14 rectangles, regularly spaced along the interface. The thickness of the first layer equal $1.75\ 10^{-3}$. The remaining subdomain is meshed with 3098 triangular meshes, with 40 mesh points regularly spaced on each domain boundary and with 23 mesh points set on each part (up and down) of the symmetry axis.

It is observed that this choice of meshing configuration leads to the best compromise between the convergence quality and the number of elements. If only a triangular meshing was used, the convergence quality would not be good enough even with very small meshes in the interface zone. A rectangular meshing only would lead to good convergence results but the number of elements required using this mesh shape would be too high and would lead to meshing errors at the center of the droplet. Moreover, it was verified that further refinement of this meshing configuration does not influence the simulation results.

3.2. Numerical procedure

According to the assumptions (see section 2.1), the mass transfer has no influence on the liquid flow; the momentum transport and the mass transport can be solved in a segregated way. For each step, the direct solver UMFPACK is used.

The steady Navier-Stokes and continuity equations (Eqs. (2)-(7)) are first solved without mass transfer using the interface and boundary conditions (Eqs. (8)-(10) and (11)-(15), respectively). The initial guess is no flow and the pressure is set to zero in both phases:

$$u_g = 0\,, v_g = 0\,, p_g = 0 \quad (28)$$

$$u_l = 0\,, v_l = 0\,, p_l = 0 \quad (29)$$

The resulting computed flows are then stored.

In the case of a simulation of the physical absorption, the diffusion-convection problem is solved without chemical reaction. Only Eqs. (16) and (17) are solved with $\psi = 0$, using the flow fields calculated at the previous step, the interface and boundary conditions (Eqs. (20)-(21) and (23)-(24), respectively) and the initial conditions (Eqs. (25)-(26)). Note that the concentrations of B does not vary in this case and remains equal to its initial value (Eq. (27)).

In the case of a simulation of an absorption coupled with a chemical reaction, the convection-diffusion-reaction problem (Eqs. (16)-(18) with ψ calculated by Eq. (19)) is solved, using the flow fields from the first step, the interface and boundary conditions (Eqs. (20)-(22) and (23)-(24), respectively) and the initial conditions (Eqs. (25)-(27)).

3.3. Post-processing and engineering aspects

The dimensionless flow and concentration fields obtained by the numerical resolution enables the calculation of some macroscopic data characterizing the flow and the dynamics of the mass transfer.

Since these data are calculated by the shell integration of the computed flow and concentration fields, a polar coordinate system (R,θ) is introduced for the sake of clarity. R is the radial coordinate and θ is the polar coordinate (from the top pole to the bottom pole of the droplet). The presented post-processed data are therefore calculated using this coordinate system.

The drag coefficient C_D is calculated from the total drag force F_D exerted by the gas phase on the droplet using the classical definition $C_D = 8F_D/\pi d_d^2 \rho_g U^2$. This drag force is calculated by the shell integration of the *z*-component of the stress on the droplet interface. It can be demonstrated that C_D is given by:

$$C_D = 4\int_0^{\pi} \tau_z(\theta) \sin\theta \, d\theta \tag{30}$$

where $\tau_z(\theta)$ is the *z*-component of the dimensionless stress exerted by the gas on the droplet interface, which is calculated by:

$$\tau_z(\theta) = \left(-p_g\big|_\theta + \frac{2}{\mathrm{Re}}\frac{\partial v_g}{\partial z}\Big|_\theta\right) n_z(\theta) + \frac{1}{\mathrm{Re}}\left(\frac{\partial v_g}{\partial r}\Big|_\theta + \frac{\partial u_g}{\partial z}\Big|_\theta\right) n_r(\theta) \tag{31}$$

where $(n_r(\theta), n_z(\theta))$ is the unit vector normal to the interface (directed towards the gas) at the considered point.

In order to monitor the mass absorption process over time, a saturation level of the droplet $\phi(t)$ is followed. It is defined as the ratio between the absorbed amount of A at the time t over the maximum amount of A that the droplet can absorb. $\phi = 0$ at $t = 0$ and $\phi = 1$ when the droplet cannot absorb more of the component A.

$\phi(t)$ can be evaluated using spatially-averaged dimensionless concentrations in the droplet at the time t, written $\langle C_\xi \rangle_t$, where $\xi = A, B$. $\langle C_\xi \rangle_t$ is given by:

$$\langle C_\xi \rangle_t = 12\int_0^{R_d}\int_0^{\pi} C_\xi\big|_{R,\theta,t} R^2 \sin\theta \, dR \, d\theta \tag{32}$$

where $R_d = 0.5$ is the dimensionless radius of the droplet.

In the case of a physical absorption, $\phi(t)$ is calculated by:

$$\phi(t) = \frac{\langle C_A\rangle_t - \alpha}{1-\alpha} \tag{33}$$

In the case of an absorption coupled with a chemical reaction, the absorbed A can be accumulated in the droplet or can be consumed by the reaction with B. The presence of B increases the droplet absorption capacity. The droplet can become saturated of A only if all the B is consumed. Therefore, $\phi(t)$ is calculated by:

$$\phi(t) = \frac{(\langle C_A\rangle_t - \alpha) + \chi^{-1}(1 - \langle C_B\rangle_t)}{1 - \alpha + \chi^{-1}} \tag{34}$$

Concerning the evaluation of the mass transfer rate, the local dimensionless flux density of A at the time t on a point of the droplet interface located by θ is computed by:

$$j_A(t,\theta) = \frac{\partial C_A}{\partial r}\Big|_{t,\theta} n_r(\theta) + \frac{\partial C_A}{\partial z}\Big|_{t,\theta} n_z(\theta) \tag{35}$$

The dimensionless total flux of A across the overall droplet interface at the time t is then calculated by:

$$J_A(t) = \frac{\pi}{2}\int_0^{\pi} j_A(t,\vartheta) \sin\theta \, d\theta \tag{36}$$

The Sherwood number at time t, $\mathrm{Sh}(t)$, which is a dimensionless mass transfer coefficient, is evaluated by dividing $J_A(t)$ by the product of the dimensionless droplet surface area (equal to π) and the dimensionless mass

transfer driving force at time t. This driving force is the difference between the maximum dimensionless concentration of A in the droplet (equal to 1) and $\langle C_A \rangle_t$. Therefore, the instantaneous Sherwood number at time t reads:

$$\mathrm{Sh}(t) = \frac{J_A(t)}{\pi(1-\langle C_A \rangle_t)} \tag{37}$$

It is more common in engineering to describe the mass transfer efficiency by Sherwood number averaged over the absorption time. The time-averaged Sherwood number $\overline{\mathrm{Sh}}$ over a dimensionless fall time t_f is calculated by:

$$\overline{\mathrm{Sh}}(t_f) = \frac{1}{t_f}\int_0^{t_f} \mathrm{Sh}(t)\,dt \tag{38}$$

In the case of a physical absorption, the concentration variation of A in the droplet is directly related to the mass transfer rate. By expressing a mass balance, the following equation can be written:

$$J_A(t) = \frac{\pi}{6}\mathrm{Pe}\frac{d\langle C_A \rangle}{dt}\bigg|_t \tag{39}$$

The time-averaged Sherwood number $\overline{\mathrm{Sh}}$ (defined by Eq. (38)) is calculated using Eq. (39) in Eq. (37), leading to:

$$\overline{\mathrm{Sh}}(t_f) = \frac{\mathrm{Pe}}{6\,t_f}\log\left(\frac{1-\alpha}{1-\langle C_A \rangle_{t_f}}\right) \tag{40}$$

According to the expression of ϕ in the physical absorption case (see Eq. (33)), the following relation between $\overline{\mathrm{Sh}}(t_f)$ and $\phi(t_f)$ is immediately deduced:

$$\overline{\mathrm{Sh}}(t_f) = \frac{\mathrm{Pe}}{6\,t_f}\log\left(\frac{1}{1-\phi(t_f)}\right) \tag{41}$$

In the results section, $\overline{\mathrm{Sh}}(t_f)$ is presented as a function of the Fourier number $\mathrm{Fo} = 4\,t_f/\mathrm{Pe}$ (such as in [9, 17, 18, 10]), for various Re and various Ha. Using the Fourier number enables the comparison of the different regimes considered with a "normalized" dimensionless time scale, since the characteristic time scales of the different cases can vary in a large range (the investigated Reynolds number variation in this study lies on 4 order of magnitude).

Note that the Fourier number of a droplet can be related to the fall distance covered by this droplet. By the definitions of the reference time and the Fourier number, the value of Fo reached after a dimensional fall distance L_f is given by the following expression:

$$\mathrm{Fo} = \frac{4\,L_f\,\eta^*}{d_d\,\mathrm{Re}\,\mathrm{Sc}\,\rho^*} \tag{42}$$

Knowing C_D for a given $\mathbf{Re}$, a force balance enables to calculate the dimensional droplet diameter d_d, which leads to the following equation:

$$d_d = \sqrt[3]{\frac{3}{4}\frac{\eta_g^2 C_D \mathbf{Re}^2}{\rho_g(\rho_l-\rho_g)g}} \quad (43)$$

where g is the gravity acceleration. Therefore, the value of $\mathbf{Fo}$ reached by a droplet after a fall of L_f can be evaluated if its Reynolds number and its drag coefficient are known. For instance, in the experimental device of Amokrane and Caussade [20] where the fall height was 1 m, a droplet with a diameter of 1 mm ($\mathbf{Re}$ close to 250) reached the bottom at $\mathbf{Fo}$ = 2 10^{-3}. For droplets with a diameter smaller than 0.15 mm ($\mathbf{Re}$ < 4), Fo was beyond 1 at the device bottom.

4. Results and discussion

4.1. Validation of the flow field

The numerical simulation results are first compared with literature correlations for the drag coefficient. Since droplets having a diameter below 1 mm can be considered as rigid spheres as far as the gas flow is concerned, the computed drag coefficient is compared with correlations for a rigid sphere cited in [21]: Lapple (Eq. L3 of Table 5.1), Schiller and Naumann (Eq. S1 of Table 5.1), and the experimental values presented in their Tables 5.2 and 5.6. The results are presented in Fig. 3 for Reynolds number varying from $\mathbf{Re}$ = 0.02 to $\mathbf{Re}$ = 250. The result corresponding to the Stokes'law ($C_D = 24/\mathbf{Re}$) is also presented.

Fig. 3

It is observed that the calculated drag coefficients are in good agreement with the literature correlations for the range of Reynolds number used, though they tend to be slightly larger than the correlations for $\mathbf{Re} \to 0$. According to these results, the numerical flow fields are considered to be validated.

Note that this good agreement with correlations developed for rigid sphere shows that the gas flow is well estimated by solving only the momentum equations

in the gas phase (Eqs. (2)-(4)), imposing a velocity equal to zero at the droplet interface. However, it is essential to compute the flows simultaneously in the gas and liquid phases (Eqs. (2)-(7)), with the appropriate conditions at the droplet interface (Eqs. (8)-(10)), to determine the flow induced in the droplet by its fall in the gas.

4.2. Physical absorption

Droplets having a Reynolds number up to 250 are considered. Typical values for an air-water system are used. The used density and viscosity ratios are $\rho^* = 830$ and $\eta^* = 55$, respectively. It is assumed that the gas component is highly soluble in the liquid, i.e. $h = 1$ is selected. The diffusivity ratio between the gas the and liquid phases is $\beta_g = 10^3$ and the Schmidt number is $\mathrm{Sc} = 500$. It is considered that, at the initial state, the concentration of A is zero in the droplet: $\alpha = 0$.

During the simulation of the transient mass absorption, the level of saturation ϕ is monitored. When ϕ reaches 0.9999, the simulation is stopped in order to prevent the computation of an undetermined $\overline{\mathrm{Sh}}$. Indeed, close to the saturation, the mass transfer driving force tends to zero as well as the mass transfer rate.

In order to follow the absorption process evolution over time for the various cases, the time evolution of ϕ and $\overline{\mathrm{Sh}}$ are presented as a function of Fo in Fig. 4 for several Reynolds number values. Note that it is verified for $\overline{\mathrm{Sh}}$ that Eq. (38) leads to the same results than Eq. (41).

Fig. 4

It is observed in Fig. 4-b that for $\mathrm{Fo} \to 0$, all the curves converge to a single curve (called hereafter LC_0), meaning that the mass transfer rate is independent of the Reynolds number. The mass transfer rate is controlled only by the diffusion in the vicinity of the interface. For $\mathrm{Fo} \to \infty$, all the curves converge to another single curve (called hereafter LC_∞), distinct from LC_0. For intermediate Fo, a sudden change in the time evolution of $\overline{\mathrm{Sh}}$ (as well in the time evolution of ϕ in Fig. 4-a) is observed, after a time decreasing as the Re increases. This change reflects a transition in the limiting step of the mass transport mechanism.

The time evolution of the concentration field of A in the droplet is examined in detail for three Reynolds number values: Re = 0.1, Re =5 and Re = 200.

At Re = 0.1, the dimensionless concentration field of A is presented for two Fo in Fig. 5.

Fig. 5

In this case, it seems that the mass absorption is dominated by the diffusive transport of A in the droplet, as the time evolution of the concentration field is very close to what would be observed in a purely diffusive process.

The dimensionless concentration field of A is presented for four Fo values at Re=5 in Fig. 6.

Fig. 6

It is observed that the absorbed component A is simultaneously transported by convection in the periphery of the droplet from the lower pole to the upper pole and penetrates in the droplet by diffusion. In this case, it seems that the convective and diffusive transport have the same order of magnitude.

The dimensionless concentration field of A is presented for four Fo values at $Ra = 200$ in Fig. 7.

Fig. 7

It can be observed that the absorbed component A is, in a first stage, mainly transported by convection in the periphery of the droplet from the lower to the upper pole. A starts to penetrate in the vortex interior only after the vortex periphery almost reaches saturation in A. A penetrates then gradually from the vortex periphery towards the interior by a mainly diffusive process.

Based on this result analysis, it can be concluded that three different steps can be observed during the overall absorption process. The first step is purely

diffusive, as demonstrated by the fact that for any $\mathbf{Re}$, the behavior at sufficiently small time is given by a single curve ($\mathbf{LC_0}$), independent of $\mathbf{Re}$. The reason why convection is not directly effective is probably that when the boundary layer is very thin, it is uniform along the interface, such that convection affects the concentration distribution only at the poles. Anyway, this first step is short in practice, especially for large Reynolds number. During the second step, the convection begins to deplete this boundary layer, first at the upper pole, the boundary layer becomes less saturated and this enhances the transfer. That moment corresponds to the sharper increase of $\phi(t)$ and the less pronounced decrease of $\overline{\mathbf{Sh}}$. In the third step, this enhancement then stops after a certain time, when the liquid richer in component A starts to reach the lower pole. At this moment, the "loop is closed", and the concentration of A in the periphery of the vortex re-increases, progressively saturating the interfacial region and decreasing the transfer. Consequently, the transfer rate is again limited by the diffusion of the component A accumulated in the periphery, towards the vortex interior.

The identification of these three successive limiting steps for the mass transfer rate enables us to propose simplified mechanisms to describe the mass transfer rate evolution for any $\mathbf{Re}$.

For $\mathbf{Re} \to \mathbf{0}$, only the first step is observed. In this case, the convective contribution to the mass transport becomes negligible and the mass absorption is dominated by the diffusive transport in the droplet. The mass transfer in the droplet can therefore be modeled assuming the purely diffusive mass transport in a stagnant liquid droplet, which writes:

$$\frac{\partial C_A}{\partial t} = \frac{1}{\mathbf{Re}} \frac{1}{r^2} \frac{\partial}{\partial r}\left(r^2 \frac{\partial C_A}{\partial r}\right) \tag{44}$$

Using Eq. (25) as initial condition and using $C_A|_{t,r=1} - 1$ and $\left.\frac{\partial C_A}{\partial r}\right|_{t,r=0} = 0$ as boundary conditions, Eq. (44) can be solved analytically and the solution reads:

$$C_A(t,r) = 1 + (1-\alpha)\sum_{i=1}^{\infty}(-1)^i \frac{2R_d}{i\pi r}\sin\left(\frac{i\pi r}{R_d}\right)\exp\left(-\frac{1}{\mathrm{Fe}}\left(\frac{i\pi}{R_d}\right)^2 t\right) \quad (45)$$

By spatially averaging Eq. (45) and expressing it as a function of Fo, the following expression can be written:

$$\langle C_A\rangle|_{\mathrm{Fo}} = 1 - (1-\alpha)\frac{6}{\pi^2}\sum_{i=1}^{\infty}\frac{1}{i^2}\exp(-(i\pi)^2\mathrm{Fo}) \quad (46)$$

Therefore, using Eq. (41) and by injecting Eq. (46) in Eq. (33), $\overline{\mathrm{Sh}}$ can be estimated as a function of Fo by the following analytical expression:

$$\overline{\mathrm{Sh}}_{\mathrm{stagnant}}(\mathrm{Fo}) = -\frac{2}{3}\frac{1}{\mathrm{Fo}}\log\left(\frac{6}{\pi^2}\sum_{i=1}^{\infty}\frac{1}{i^2}\exp(-(i\pi)^2\mathrm{Fo})\right) \quad (47)$$

Note that this expression tends to $\overline{\mathrm{Sh}}_{\mathrm{stagnant}} = 2\pi^2/3$ for $\mathrm{Fo} \to \infty$.

For $\mathrm{Re} \to \infty$, the third step is directly observed. The vortex periphery can be considered as instantaneously saturated and the mass absorption is controlled by the diffusive transport within the vortex. The vortex zone, in the three-dimensional droplet, has the form of a ring torus. If this torus is transversally cut and unfold along the longitudinal direction, the generated volume is a cylinder. The absorbed mass which has to penetrate by a mainly diffusive process through this toroidal vortex can then be modeled by the diffusive mass transport through a cylinder along the cylinder radius coordinate r_{cyl} with an imposed concentration at its surface. This model equation writes:

$$\frac{\partial C_A}{\partial t} = \frac{1}{\mathrm{Fe}}\frac{1}{r_{\mathrm{cyl}}}\frac{\partial}{\partial r_{\mathrm{cyl}}}\left(r_{\mathrm{cyl}}\frac{\partial C_A}{\partial r_{\mathrm{cyl}}}\right) \quad (48)$$

Using Eq. (25) as initial condition and using $C_A|_{t,r_{\mathrm{cyl}}=1} = 1$ and $\left.\frac{\partial C_A}{\partial r_{\mathrm{cyl}}}\right|_{t,r_{\mathrm{cyl}}=0} = 0$ as boundary conditions, Eq. (48) can be solved analytically and the solution reads:

$$C_A(t,r_{\mathrm{cyl}}) = 1 - (1-\alpha)\sum_{i=1}^{\infty}\frac{\gamma_i}{\zeta_i}J_0\left(\lambda_i\frac{r_{\mathrm{cyl}}}{R_{\mathrm{cyl}}}\right)\exp\left(-\frac{\lambda_i^2}{R_{\mathrm{cyl}}^2}\frac{t}{\mathrm{Fe}}\right) \quad (49)$$

where R_{cyl} is the dimensionless radius of the cylinder equivalent to the torus formed by the vortex zone, λ_i is the i^{th} zero of the zero-order Bessel function of the first kind J_0, $\gamma_i = \int_0^1 xJ_0(\lambda_i x)dx$ and $\zeta_i = \int_0^1 x(J_0(\lambda_i x))^2 dx$.

The spatially-averaged concentration of A over the cylinder volume, expressed as a function of the Fourier number, writes then:

$$\langle C_A\rangle_{\mathrm{cyl}}\big|_{\mathrm{Fo}} = 1 - (1-\alpha)\sum_{i=1}^{\infty}\frac{2\gamma_i^2}{\zeta_i}\exp\left(-\lambda_i^2\left(\frac{R_d}{R_{\mathrm{cyl}}}\right)^2\mathrm{Fo}\right) \quad (50)$$

Let V_{cyl} be the dimensionless volume of the cylinder equivalent to the torus formed by the vortex zone. Since the vortex periphery is considered as instantaneously saturated (with $C_A = 1$ in this zone), the spatially-averaged concentration of A in the overall droplet is related to the spatially-averaged

concentration in the torus modeled by the cylinder by $V_d\langle C_A\rangle = V_{cyl}\langle C_A\rangle_{cyl} + (V_d - V_{cyl})$. Therefore, the spatially-averaged concentration of A over the droplet volume writes:

$$\langle C_A\rangle|_{Fo} = 1 - (1-\alpha)\frac{V_{cyl}}{V_d}\sum_{i=1}^{\infty}\frac{2\gamma_i^2}{\zeta_i}\exp\left(-\lambda_i^2\left(\frac{R_d}{R_{cyl}}\right)^2 Fo\right) \quad (51)$$

Using Eq. (41) and by injecting Eq. (51) in Eq. (33), $\overline{Sh}$ can be estimated as a function of Fo by the following analytical expression:

$$\overline{Sh}_{cyl}(Fo) = -\frac{2}{3}\frac{1}{Fo}\log\left(\frac{V_{cyl}}{V_d}\sum_{i=1}^{\infty}\frac{2\gamma_i^2}{\zeta_i}\exp\left(-\lambda_i^2\left(\frac{R_d}{R_{cyl}}\right)^2 Fo\right)\right) \quad (52)$$

This equation tends to $\overline{Sh}_{cyl} = \frac{2}{3}\lambda_1^2\left(\frac{R_d}{R_{cyl}}\right)^2$ for $Fo \to \infty$. R_{cyl} and V_{cyl} are adjustable parameters of the model and their values are estimated by the comparison with the curve LC_∞ of Fig. 4-b. R_{cyl} is estimated to $R_d/2.4$ and V_{cyl} is estimated to $0.97V_d$. Note that these fitted values are geometrically coherent for a ring torus contained in a spherical droplet.

For intermediate Re and limited Fo, it is observed during the initial stage of the mass absorption that the mass transfer rate is limited by the penetration in the vicinity of the interface, i.e. by a diffusive mechanism. A thin layer of liquid in contact with the interface can then be considered as a film and the width of this layer depends on the toroidal vortex angular velocity, which decreases as the Reynolds number increases. Therefore, the penetration-film model of Toor and Marchello [26] is proposed to model the mass transfer rate before the saturation of the vortex periphery. The mass transport equation writes:

$$\frac{\partial C_A}{\partial t} = \frac{1}{Pe}\frac{\partial^2 C_A}{\partial x^2} \quad (53)$$

where x is the dimensionless distance normal to the interface, oriented to the droplet interior ($x = 0$ at the interface). Let δ_f be the dimensionless film thickness of the model (i.e. the ratio of the dimensional film thickness over the dimensional droplet diameter). Eq. (53) is solved analytically using $C_A(x, t=0) = \alpha$ as initial conditions and $C_A(x=0, t) = 1$ and $C_A(x=\delta_f, t) = \alpha$ as boundary conditions. The solution reads:

$$C_A(x,t) = \alpha + (1-\alpha)\sum_{i=0}^{\infty}\left(\mathrm{erfc}\left(\frac{(2i\delta_f + x)\sqrt{Pe}}{2\sqrt{t}}\right) - \mathrm{erfc}\left(\frac{(2(i+1)\delta_f - x)\sqrt{Pe}}{2\sqrt{t}}\right)\right) \quad (54)$$

The mass flux density is then calculated by:

$$j_A(t) = -\left.\frac{\partial C_A}{\partial x}\right|_{x=0,t} = \sqrt{\frac{Pe}{\pi t}}\left(1 + 2\sum_{i=1}^{\infty}\exp\left(-\frac{i^2\delta_f^2 Pe}{t}\right)\right) \quad (55)$$

Using $J_A(t) = 4\pi R_d^2 j_A(t)$, $Sh(t) = J_A(t)/(\pi(1-\alpha))$ and the definition of $\overline{Sh}$ (see Eq. (38)), $\overline{Sh}$ can then be estimated as a function of Fo by the following analytical expression:

$$\overline{Sh}_{PF}(Fo) = \frac{4}{\sqrt{\pi Fo}}\left(1 + 2\sum_{i=1}^{\infty}\left(\exp\left(-\frac{i^2\delta_f^2}{Fo}\right) - \sqrt{\frac{\pi i^2\delta_f^2}{Fo}}\,\mathrm{erfc}\left(\sqrt{\frac{i^2\delta_f^2}{Fo}}\right)\right)\right) \quad (56)$$

δ_f is an adjustable parameter of this model. The values of δ_f are estimated for various Re (between 1 and 250) by fitting the curves computed using Eq. (56) with

the initial part (i.e. before the transition to the third step) of the $\overline{Sh}$ curves in Fig. 4-b.

It is observed that the values obtained for δ_f decrease as Re increases. It is found that δ_f can be correlated to Re by the following expression:

$$\delta_f = 0.1825\ Re^{-0.597} \quad (57)$$

To summarize, thanks to these analysis, $\overline{Sh}$ for a droplet with a given Re can be estimated at any Fo using analytical expressions. For $Re < 1$, $\overline{Sh}$ can be approached by $\overline{Sh}_{stagnant}$, given by Eq. (47). For $Re > 1$, $\overline{Sh}$ can be approached by $\overline{Sh}_{PF}$, given by Eq. (56) and using Eq. (57), during the initial stage and then by Sh_{cyl}, given by Eq. (52), when the vortex periphery is saturated. The transition is reached when $\overline{Sh}_{PF}$ becomes larger than $\overline{Sh}_{cyl}$. In other words, $\overline{Sh}$ can be approached by: $\min\left[\overline{Sh}_{cyl}(Fo), \overline{Sh}_{PF}(Re, Fo)\right]$.

The time evolution of the analytical approximations of $\overline{Sh}$ are presented in Fig. 8 and superimposed to the numerical simulation results. Eq. (47) is used for $Re \to 0$, $\min\left[\overline{Sh}_{cyl}(Fo), \overline{Sh}_{PF}(Re, Fo)\right]$ is used for Re between 1 and 250, and Eq. (52) is used for $Re \to \infty$. The analytical expressions are presented in solid lines and the numerical simulation results are presented in dashed lines. It is observed that the analytical expressions agree very well with the numerical simulation results.

Fig. 8

To end this section, a last comment is done on the curve presented in Fig. 4-b. For $Re > 1$, it seems that the Fourier number at which the transition occurs is proportional to $1/Re$. It would mean that the transition occur at a Fourier number proportional only to the number of diameter that the droplet has covered during its fall (when the "loop is closed"). For a given physico-chemical system, this number would be constant and independent of the droplet size. This point will be analyzed in details in a future work.

4.3. Mass absorption enhanced by chemical reaction

In this section is studied the effect of a chemical reaction on the mass transfer rate, for various Reynolds and Hatta numbers. The initial concentration of B is considered in excess compared to the concentration of A at saturation, as it is the case in the industrial practice. $[B]_0$ is chosen as ten times larger ($\chi = 0.1$) than $[A]_{eq}$. The simulations are realized for four values of the Reynolds number, corresponding to the different regimes which have been described for the physical absorption: Re = 0.1, Re =1, Re =10 and Re = 100. For each value of the Reynolds

number, three values of the Hatta number, corresponding to different chemical regimes, are considered: Ha = 0.1, Ha = 1 and Ha = 10. The same values than those chosen in the previous section are used for ρ^* , η^*, Sc, β_g, h and α. It is considered that the diffusion coefficient of the reactant B is smaller than the diffusion coefficient of A, then $\beta_b = 0.5$ is selected.

The effect of a chemical reaction on the mass transfer rate and the saturation evolutions, for various Reynolds and Hatta numbers are presented in the following figures. The time evolution of $\overline{\mathrm{Sh}}$ and of ϕ as functions of Fo for the three values of Ha are presented and compared with the physical absorption case in Figs. 9, 11, 13 and 15 for Re = 0.1, Re = 1, Re = 10 and Re = 100, respectively. The dimensionless concentration fields of A and B, for the three values of Ha, are presented at $\mathrm{Fo}=10^{-1}$ in Fig. 10, at $\mathrm{Fo}=10^{-1}$ in Fig. 12, at $\mathrm{Fo}=10^{-2}$ in Fig. 14 and at $\mathrm{Fo}=10^{-3}$ in Fig. 16, for Re =0.1, Re = 1, Re = 10 and Re = 100, respectively.

Fig. 9

Fig. 10

Fig. 11

Fig. 12

Fig. 13

Fig. 14

Fig. 15

Fig. 16

For Ha = 0.1, it is observed in Figs. 9-a, 11-a, 13-a and 15-a that the presence of B has a significant influence on the time evolution of ϕ. The saturation of the

droplet is delayed and it is observed that this delay increases as the Reynolds number decreases. By contrast, it is observed that the presence of the chemical reactant does not have a significant influence on the mass transfer rate. Indeed, the time evolution of $\overline{Sh}$ is always close to the evolution observed for physical absorption, as it can be observed in Figs. 9-b, 11-b, 13-b and 15-b. A slight enhancement is observed after $Fo=10^{-3}$ only for the case Re = 100 (Fig. 15-b).

Note that it might seem surprising that the effect of the chemical reaction is so pronounced on the evolution of the saturation ϕ (see Fig. 9-a), especially for small values of Ha, while it has only a very small impact on $\overline{Sh}$ (see Fig. 9-b). Actually, even though the overall rate of absorption is almost unchanged by the chemical reaction when the latter is slow, ϕ is calculated in a different way than in the physical absorption case, i.e. the full storage capacity of the droplet is now considered (see the difference in Eqs. (33) and (34), the latter incorporating the additional storage capability due to chemical conversion by reaction with the reactant B, which increases as χ decreases).

On the one hand, the analysis of the concentration fields of B (in Figs. 10, 12, 14 and 16) shows that, for any Re, the concentration of B decreases gradually in the droplet but its concentration field remains almost homogeneous. On the other hand, it is observed that the evolutions of the concentration fields of A with Re are similar to those observed in the physical absorption case. Therefore, the mass transfer rate remains controlled only by the mass transport of A but the saturation is delayed by the presence of B.

For Ha = 1, it appears that the time evolutions of $\overline{Sh}$ and ϕ with Fo is determined by a combination of the phenomena controlling the mass transfer for Ha = 0.1 and Ha = 10 (analyzed hereunder), especially by the coupling of the transports of A and B. Indeed, for any Re, an intermediate situation between the cases Ha = 0.1 and Ha = 10 is observed for the considered Re.

For Ha = 10, it is observed in the time evolution of ϕ for any Re (see Figs. 9-a, 11-a, 13-a and 15-a) that the saturation is always reached around the same Fourier number than in the physical absorption case. By contrast, significantly different behaviors are observed for the time evolution of $\overline{Sh}$, depending on Re.

For Re = 0.1, it is observed in Fig. 9-b that the mass transfer rate is higher than in the physical absorption case, especially around $Fo=10^{-3}$, but it tends to be

the same than in the physical absorption case for $\mathrm{Fo} \to 0$. The analysis of the concentration fields of A and B (see the right part of Fig. 10) shows that A is depleted by its consumption in the reaction. The concentration of A close to the interface cannot increase as long as B is present in this zone, maintaining a high concentration gradient of A near the interface and enhancing the mass transfer rate. For this value of Re, it has been shown that the mass transport mechanism is mostly diffusive. Therefore, the mass transfer rate is mostly controlled by the diffusive transport of B in a first stage, and it becomes controlled by the diffusive transport of A in a second stage, when B is depleted.

For Re = 1, it is observed in Fig. 11-b that the mass transfer rate becomes significantly higher than in the physical absorption, until the droplet is close to the saturation (see the corresponding Fo in Fig. 11-a). The analysis of the concentration fields of A and B (right part of Fig. 12) reveals that the mass transfer rate is controlled by the transport of B in a first stage, and it becomes controlled by the transport of A in a second stage, but this time the mass transport is determined by the combination of the convection and the diffusion.

For Re = 10 and Re = 100, it is observed in Figs. 13-b and 15-b that the mass transfer rate is strongly enhanced (even more for Re = 100 than for Re = 10) until the liquid is close to the saturation. A sudden change in the curve of $\overline{\mathrm{Sh}}$ is also observed around $\mathrm{Fo}=10^{-2}$ for Re = 10 and around $\mathrm{Fo}=10^{-3}$ for Re = 100, reflecting a transition in the mechanism controlling the mass transfer rate, such as in the physical absorption case. Note that these transition occur at approximately the same Fo than those observed in the physical absorption. The analysis of the concentration fields of A and B (right part of Figs. 14 and 16) shows that B is completely depleted in the periphery of the toroidal vortex. The concentration of B is still high within the vortex and the concentration of A is just starting to fill the vortex periphery. After that, the concentration of B decreases gradually within the vortex, while the concentration of A increases and the transport of A and B within the toroidal vortex is mostly diffusive. Therefore, the mass transfer rate is controlled in a first stage by the convective transport of B in the vicinity of the interface. It is strongly enhanced in a second stage by the convective transport of A

in the vortex periphery to be finally controlled by the coupling of the reaction with the diffusive transport of A and B within the vortex.

5. Conclusion and perspectives

This work has considered direct numerical simulations of the gas-droplet mass transfer of a component A in gas phase into a liquid spherical droplet in free fall. A component B is dissolved in the liquid droplet, and this component reacts with A in the liquid phase, leading to an increase of the storage capability and an enhancement of the mass transfer rate.

The mass transfer is studied by computing simultaneously the flow fields and the concentration fields in both gas and liquid phases. The analysis of the time evolution of the concentration fields for various regimes, distinguished by the Reynolds and the Hatta numbers, has enabled us to highlight the coupling between the phenomena for each regime and to identify which ones control the mass transfer rate.

In section 4.2, the physical absorption (without reaction) is studied. It is concluded from the results analysis that three different steps can be observed during the overall absorption process. The first step is purely diffusive, as demonstrated by the fact that the behavior at sufficiently small time is independent of Re. The diffusive transport is directed towards the droplet center. During the second step, the convection begins to deplete this boundary layer, first at the upper pole. The boundary layer becomes less saturated and this enhances the transfer. In the third step, this enhancement then stops after a certain time, when the liquid richer in component A starts to reach the lower pole. The concentration of A in the periphery of the vortex re-increases, progressively saturating the interfacial region and decreasing the transfer. Consequently, the transfer rate is again limited by the

diffusion of the component A accumulated in the periphery, towards the vortex inside.

For $\mathrm{Re} \to 0$, only the first step is observed. For $\mathrm{Re} \to \infty$, the third step is directly observed. For intermediate Re, the mass transfer rate is controlled successively by these three limiting steps and the time of transition between the steps decreases as Re increases.

The identification of these three successive limiting steps for the mass transfer rate enables us to propose simplified mechanisms to describe the mass transfer rate evolution for any flow regime. Based on these simplified mechanisms, analytical expressions are developed to evaluate $\overline{\mathrm{Sh}}$ as a function of Fo for any Re.

In the limit of $\mathrm{Re} \to 0$ (first step), $\overline{\mathrm{Sh}}$ is modeled by $\overline{\mathrm{Sh}}_{\mathrm{stagnant}}$ (Eq. (47)), while in the limit of $\mathrm{Re} \to \infty$ (third step), $\overline{\mathrm{Sh}}$ is modeled by $\overline{\mathrm{Sh}}_{\mathrm{cyl}}$ (Eq. (52)) (with the adjustable parameters R_{cyl} and V_{cyl} fitted to $R_d/2.4$ and $0.97V_d$, respectively).

For $\mathrm{Re} < 1$, $\overline{\mathrm{Sh}}(\mathrm{Re}, \mathrm{Fo})$ can be approached by $\overline{\mathrm{Sh}}_{\mathrm{stagnant}}(\mathrm{Fo})$. For $\mathrm{Re} > 1$, $\overline{\mathrm{Sh}}(\mathrm{Re}, \mathrm{Fo})$ can be approached by $\overline{\mathrm{Sh}}_{\mathrm{PF}}(\mathrm{Fo})$ during the initial stage (given by Eq. (56) and using the correlation (57) developed by comparison with the numerical simulation results), and later by $\overline{\mathrm{Sh}}_{\mathrm{cyl}}(\mathrm{Fo})$, when the periphery of the toroidal vortex is saturated. The transition is reached when $\overline{\mathrm{Sh}}_{\mathrm{PF}}$ becomes larger than $\overline{\mathrm{Sh}}_{\mathrm{cyl}}$, therefore $\overline{\mathrm{Sh}}(\mathrm{Re}, \mathrm{Fo})$ can be approached by $\min\left[\overline{\mathrm{Sh}}_{\mathrm{cyl}}(\mathrm{Fo}), \overline{\mathrm{Sh}}_{\mathrm{PF}}(\mathrm{Re}, \mathrm{Fo})\right]$.

It is worth mentioning that these analytical expressions are compared to the numerical simulation results (see Fig. (8)) and that an excellent agreement is observed.

In section 4.3, the influence of a chemical reaction on the mass absorption rate is investigated. In this case, the chemical reaction can enhance the mass transfer rate and can delay the saturation of the droplet, depending on the Reynolds and the Hatta number.

For $\mathrm{Ha} < 1$, it is observed that the presence of B does not have a significant influence on the mass transfer rate and it is concluded that the mass transfer rate remains mostly controlled by the mass transport of A in the droplet, as without reaction. However, the saturation is delayed by the presence of B as it increases the droplet absorption capability due to chemical conversion by reaction and the delay increases as the Reynolds number decreases.

For $\mathrm{Ha} = 1$, an intermediate situation is observed. The mass transfer rate of A also gets influenced by the transport of B in the droplet.

Finally, for $\mathrm{Ha} > 1$, the mass transfer rate is controlled by the transport of B in the droplet in a first stage. Later, it becomes controlled by the interaction between the reaction and the transport of A and B. The prevalent mass transport mechanism depends on the value of Re. For $\mathrm{Re} < 1$, the mass transport is mostly diffusive towards the droplet center. For $\mathrm{Re} = 1$, the mass transport is determined by the

combination of the convection and the diffusion. For $Re > 1$, the mass transfer rate is controlled in a first stage by the convective transport of B in the vicinity of the interface. It is controlled in a second stage by the convective transport of A in the vortex periphery and finally it is controlled by the interaction of the reaction and the diffusive transport of A and B within the vortex.

The results presented in this paper and their detailed analysis show the importance of taking into account all the phenomena simultaneously in gas-droplet mass transfer modeling. However, a further analysis of some issues for $Re > 1$ would be worth of interest, such as the observation that in the physical absorption, the value of Fo at the transition between the second and the third step seems to be proportional to $1/Re$ and the observation that the value of Fo at the transition for $Ha = 10$ seems to be the same than in the physical absorption. A criterion determining the value of Fo at the transition could be identified. It would also be full of interest to develop a simplified model incorporating the effect of chemical reaction. In the limit $Ha \to \infty$, it would be possible to determine a correlation for the mass transfer rate enhancement, based of the mass transport mechanism observed in the physical absorption for any Re, at least for the initial stage (when the mass transfer rate is controlled by the transport of B).

Another perspectives are to model the effects of the presence of surface-active contaminants and to extend this analysis to larger drops. In this latter case, it will be necessary to take into account the deformations and the oscillations of the drop interface and the turbulence in the flow fields. Several methods are available and have been described in the literature for physical absorption, such as the moving element method [8] or the level set method [27].

Acknowledgements

F.R.S.-FNRS (Belgian National Fund for Scientific Research) Postdoctoral Researcher Christophe Wylock and Senior Research Associate Pierre Colinet gratefully acknowledge the financial support from the Fund.

References

[1] C. Brogren, H. T. Karlsson, Modeling of the absorption of SO_2 in a spray scrubber using the penetration theory, Chem. Eng. Sci. 52(18) (1997) 3085-3099.

[2] A. Bandyopadhyay, M. N. Biswas, Modelling of SO_2 scrubbing in spray towers, Sci. Total Environ. 383 (2007) 25-40.

[3] S. Sarkar, B. C. Meikap, S. G. Chatterjee, Modeling of removal of sulfur dioxide from flue gases in a horizontal cocurrent gasliquid scrubber, Chem. Eng. J. 131 (2007) 263-271.

[4] M. K. Akbar, S. M. Ghiaasiaan, Modeling the gas absorption in a spray scrubber with dissolving reactive particles, Chem. Eng. Sci. 59 (2004) 967-976.

[5] T. K. Sherwood, R. L. Pigford, Absorption and extraction, McGraw-Hill, New York, 1963.

[6] R. Higbie, The rate of absorption of pure gas into a still liquid during short periods of exposure, Trans. Am. Inst. Chem. Ing. 31 (1935) 365.

[7] B. P. Leclair, A. E. Hamielec, H. R. Pruppacher, W. D. Hall, A theoretical and experimental study of the internal circulation in water drops falling at terminal velocity in air, J. Atmos. Sci. 29(4) (1972) 728-740.

[8] J. Petera, L. Weatherly, Modelling of mass transfer from falling droplets, Chem. Eng. Sci. 56 (2001) 4929-4947.

[9] B. I. Brounshtein, A. S. Zheleznyak, G. A. Fishbein, Heat and mass transfer in interaction of spherical drops and gas bubbles with a liquid flow, Int. J. Heat & Mass Transfer 13 (1970) 963-973.

[10] B. I. Broushtein, G. A. Fishbein, V. Y. Rivikind, Mass transfer accompanied by chemical conversion of substance in a drop, Int. J. Heat & Mass Transfer 19 (2) (1976) 193-199.

[11] Lamb, Hydrodynamics, 6th Edition, Dover Publications, New York, 1932.

[12] A. E. Hameliec, A. I. Johnson, Viscous flow around fluid spheres at intermediate Reynolds number, Can. J. Chem. Eng. 40 (2) (1962) 41-45.

[13] R. Kronig, J. C. Brink, On the theory of extraction from falling droplets, Appl. Sci. Res. A 2 (1950) 142-154.

[14] L. Baboolal, H. Pruppacher, J. Topalian, A sensitivity study of a theoretical model of SO2 scavenging by water drops in air, J. Atmos. Sci. 38 (1980) 856-870.

[15] T. Elperin, A. Fominykh, Conjugate mass transfer during gas absorption by falling liquid droplet with internal circulation, Atmos. Env. 39 (2005) 4575-4582.

[16] A. R. Uribe-Ramírez, W. J. Korchinsky, Fundamental theory for prediction of single-component mass transfer in liquid drops at intermediate Reynolds numbers ($10 \leq Re \leq 250$), Chem. Eng. Sci. 55(16) (2000) 3305-3318.

[17] M. Waheed, M. Henschke, A. Pfennig, Mass transfer by free and forced convection from single spherical liquid drops, Int. J. Heat & Mass Transfer 45 (22) (2002) 4507-4514.

[18] A. Paschedag, W. H. Piarah, M. Kraume, Sensitivity study for the mass transfer at a single droplet, Int. J. Heat & Mass Transfer 48 (2005) 3402-3410.

[19] M. K. Akbar, J. Yan, S. M. Ghiaasiaan, Mechanism of gas absorption enhancement in a slurry droplet containing reactive, sparingly soluble microparticles, Int. J. Heat & Mass Transfer 46 (2003) 4561-4571.

[20] H. Amokrane, B. Caussade, Gas absorption into a moving spheroidal water drop, J. Atmos. Sci. 56(12) (1999) 1808-1829.

[21] R. Clift, J. Grace, M. Weber, Bubbles, drops and particles, Dover Publications, Mineola, 1978.

[22] C. J. Walcek, H. R. Pruppacher, J. H. Topalian, S. K. Mitra, On the scavenging of SO2 by cloud and raindrops II: An experimental study of SO2 absorption and desorption for water drops in air, J. Atmos. Chem. 1 (3) (1984) 291-306.

[23] E. R. Altwicker, C. E. Lindhjem, Absorption of gases into drops, A.I.Ch.E. Journal 34(2) (1988) 329-332.

[24] P. Trambouze, J.-P. Euzen, Chemical Reactors: from design to operation, Institut Français du pétrole publications, Technip, 2004.

[25] R. B. Bird, W. E. Stewart, E. N. Lightfoot, Transport Phenomena, second Edition, John Wiley&Sons, 2002.

[26] H. L. Toor, J. M. Marchello, Film-penetration model for mass and heat transfer, A.I.Ch.E. Journal 4 (1) (1958) 97-101.

[27] K. B. Deshpande, W. B. Zimmerman, Simulation of interfacial mass transfer by droplet dynamics using the level set method, Chem. Eng. Sci. 61 (2006) 6486-6498.

List of figures

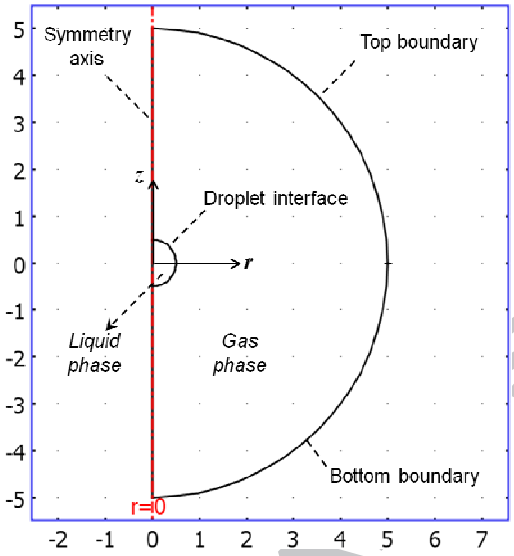

Fig. 1

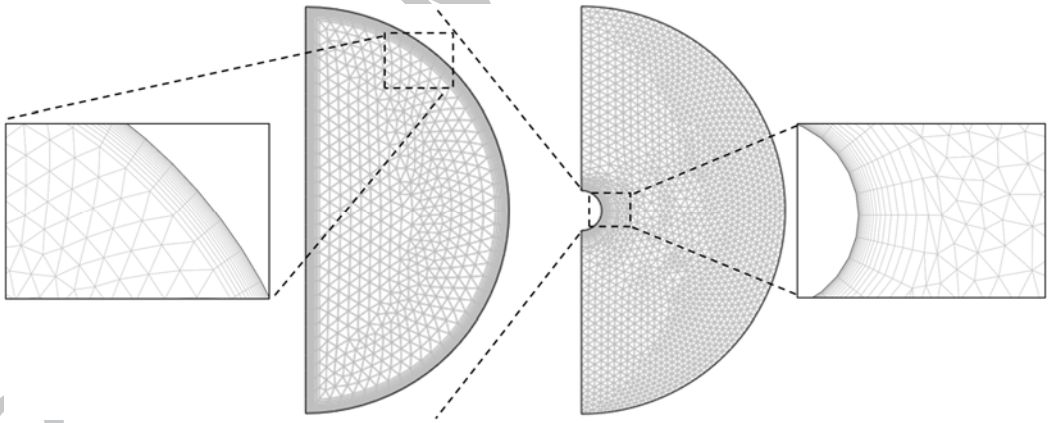

Fig. 2

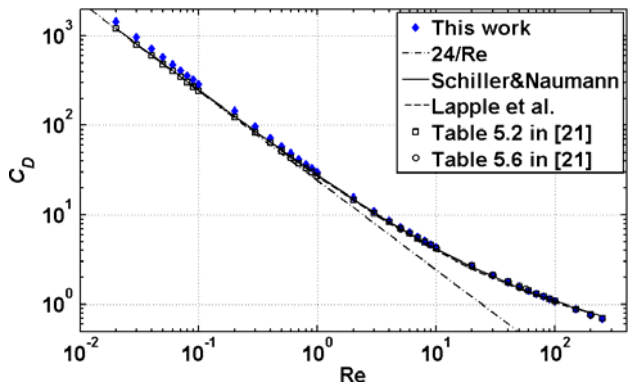

Fig. 3

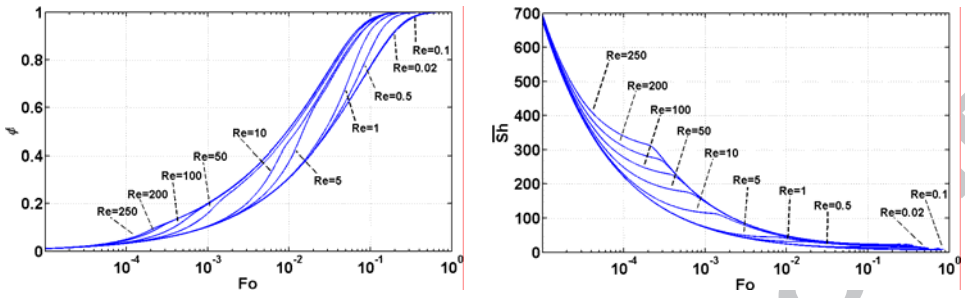

(a) (b)

Fig. 4

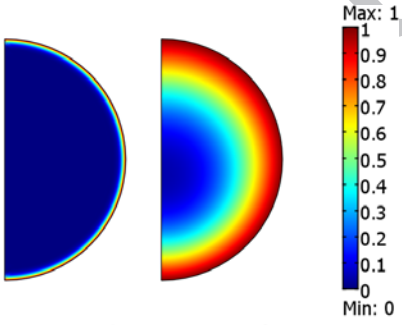

Fig. 5

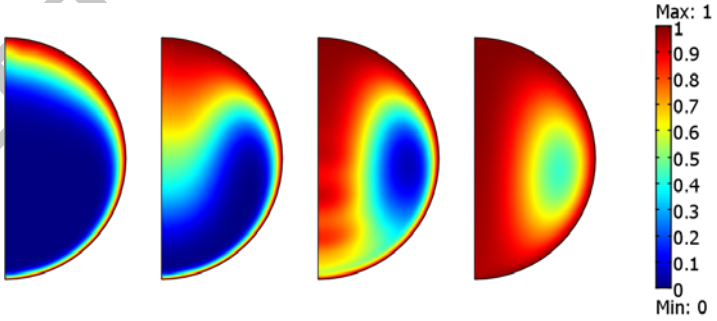

Fig. 6

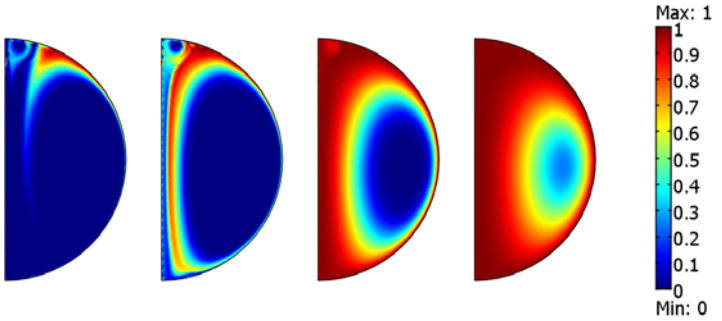

Fig. 7

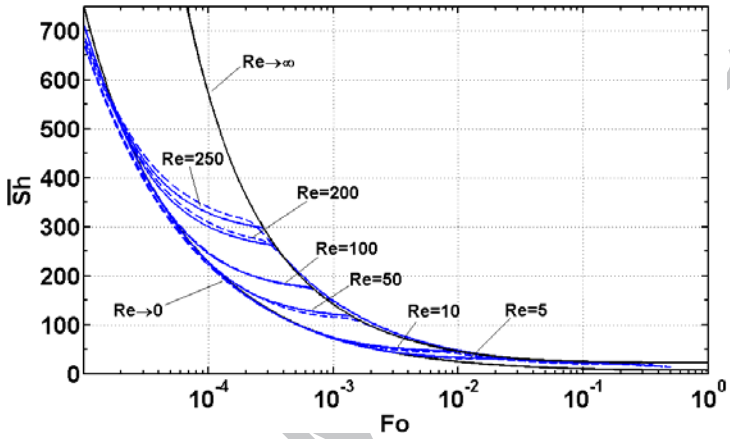

Fig. 8

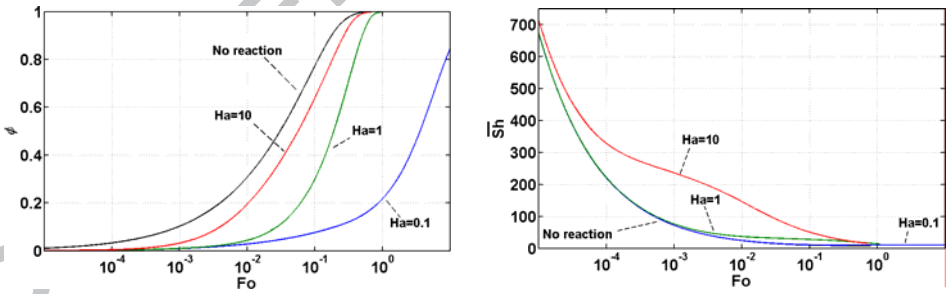

(a) (b)

Fig. 9

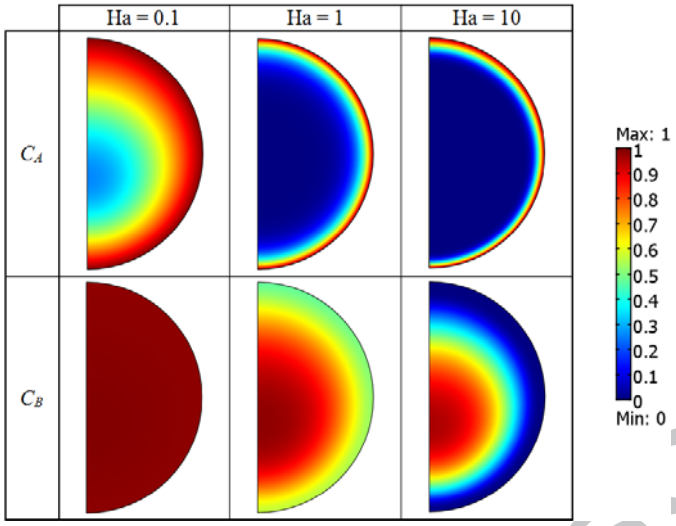

Fig. 10

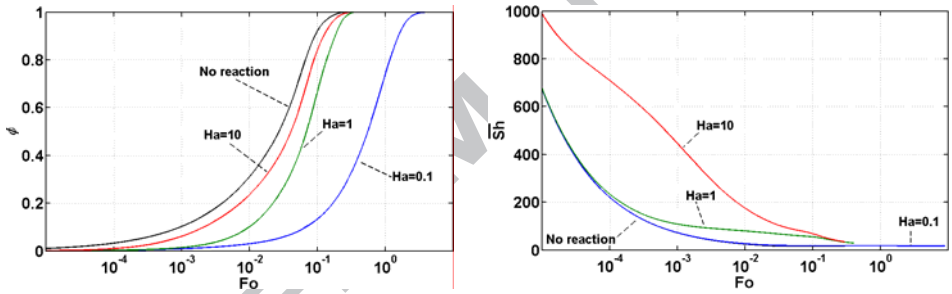

(a) (b)

Fig. 11

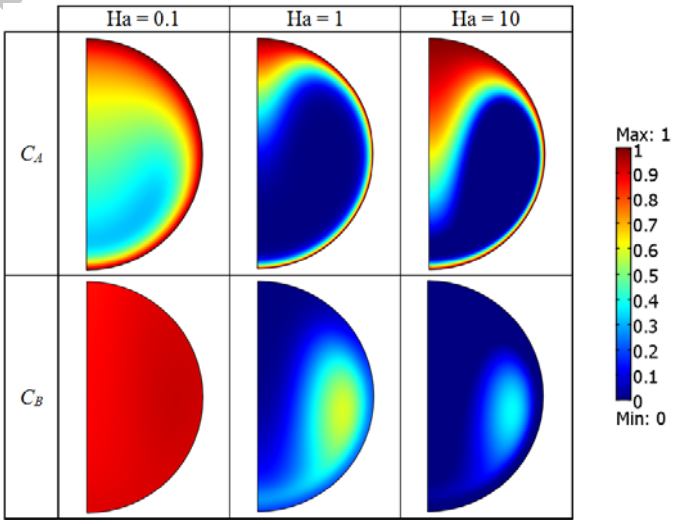

Fig. 12

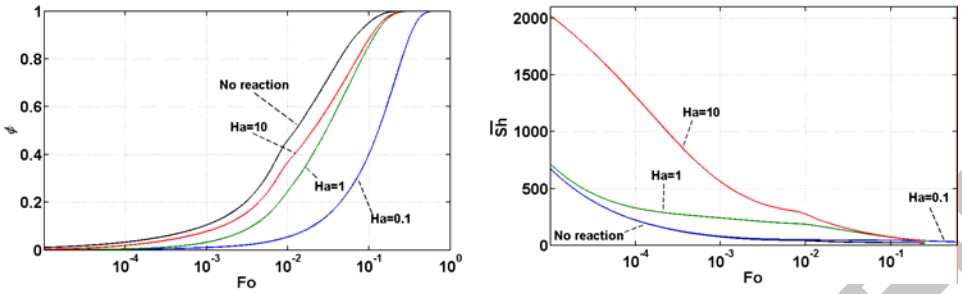

(a) (b)

Fig. 13

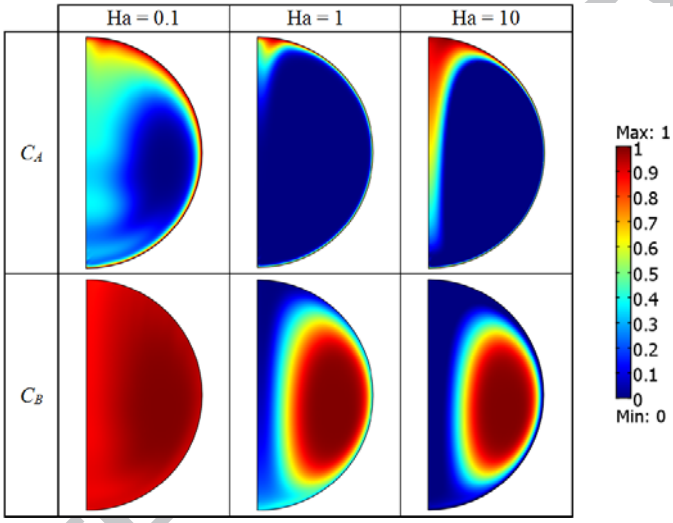

Fig. 14

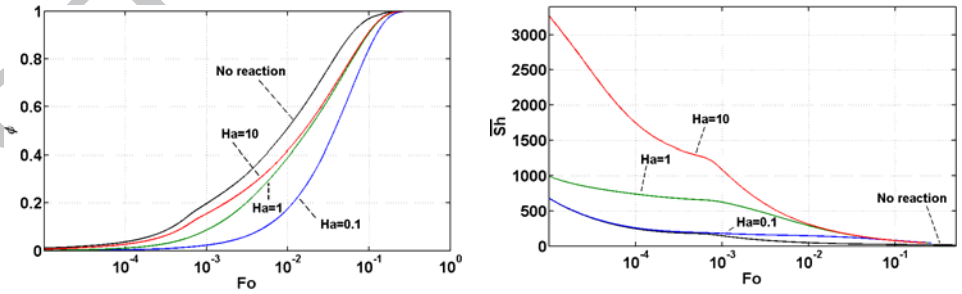

(a) (b)

Fig. 15

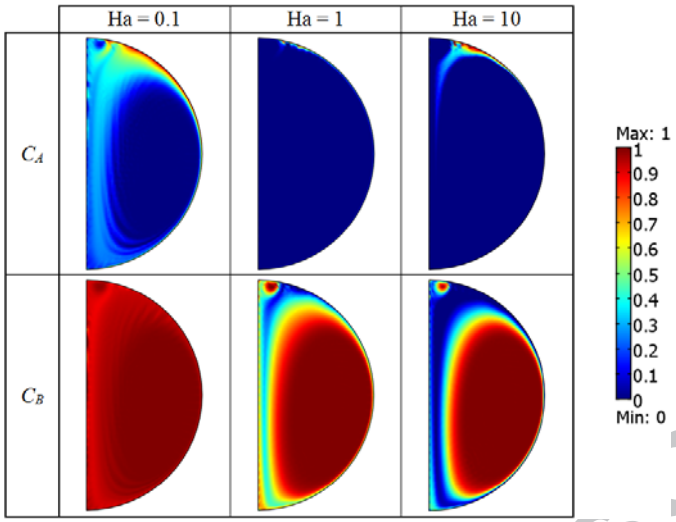

Fig. 16

> Gas-droplet mass transfer model coupling convective and diffusive mass transport and chemical reactions

> Detailed analysis of interactions between phenomena for various flow and chemical regimes

> Identification of absorption rate controlling phenomena

> New analytical expression for the mass transfer rate in the physical absorption case